AIAA JOURNAL
Vol. 37, No. 6, June 1999

Miniature Multihole Pressure Probes and Their Neural-Network-Based Calibration

Othon K. Rediniotis* and Rajesh Vijayagopal†
Texas A&M University, College Station, Texas 77843-3141

We present the development of miniature multihole pressure probes and a novel neural-network-based calibration algorithm for them. Seven-hole probes of tip diameters as low as 0.035 in. (0.9 mm) were successfully fabricated with high tip surface quality. Any of the typical probe tip geometries, i.e., hemispherical, conical, or faceted, could be fabricated. The miniature probes were calibrated and tested in a wind tunnel. A backpropagation-based neural-network calibration algorithm was developed for these probes, with flexibility in network architecture design and network self-optimization capabilities. In the feedforward mode the algorithm yields computational speeds an order of magnitude higher than those typically achieved by similar accuracy interpolation algorithms. The new algorithm has prediction accuracies of 0.28 deg in the flow angles and 0.35% in the velocity magnitude.

Nomenclature

A_s = static pressure coefficient
A_t = total pressure coefficient
B_c = cone-angle pressure coefficient
B_p = pitch-angle pressure coefficient
B_r = roll-angle pressure coefficient
B_y = yaw-angle pressure coefficient
C_p = generic pressure coefficient; could stand for any of B_p, B_c, B_y, B_r, A_t, A_s
$\boldsymbol{E}$ = error vector
$\hat{e}$ = sum-squared error
f_i^h = activation function for node i on layer h
$\boldsymbol{I}$ = identity matrix
$\boldsymbol{J}$ = error Jacobian matrix
o_i^h = output of node i on layer h
p_i = pressure reading at orifice i of the probe
p^+ = pressure reading at peripheral port adjacent to port i, in the clockwise direction when looking into the probe tip
p^- = pressure reading at peripheral port adjacent to port i, in the counterclockwise direction when looking into the probe tip
q = characteristic of dynamic pressure
w_{ij}^h = weight applied to the connection to node i on layer h from node j on layer $h-1$
x_i^h = sum of node weighted inputs
α = pitch flow angle; momentum coefficient
β = yaw flow angle
δ_i^h = error sensitivity per node
δC_p = uncertainty in the calculation of C_p
δp_i = uncertainty in the measurement of pressure p_i
η = learning rate coefficient
θ = cone flow angle
ϕ = roll flow angle

I. Introduction

OVER the years multihole probes, such as five- and seven-hole probes, have established themselves as some of the easiest-to-use and cost-effective devices for three-component velocity measurements in research as well as industry environments. They provide accurate flow measurements for flow angles up to 75 deg and are inexpensive and robust. Furthermore, to minimize flow disturbance, probes of small diameter can be fabricated. Because of their small size, irregularities in manufacturing are unavoidable, which requires that each probe be calibrated individually. Unless the probe tip is physically damaged, it will maintain its structural characteristics, and therefore only one initial calibration is required for the lifetime of the probe.

Because multihole pressure probes are intrusive flow-diagnostics instruments, concerns of probe interference with the flows they are trying to measure always arise. For example, in the case of leading-edge vortical flows over delta wings, the presence of the probe in the neighborhood of the vortex core can induce premature vortex breakdown.[1] Therefore, a strong incentive exists to reduce the probe size, thus reducing the interference. Concurrently, probe-size reduction offers higher spatial resolution for measurements in high-shear flows. Also, when measuring near a surface, a distance of at least four probe diameters should be maintained to avoid wall effects.[2] Smaller probes can measure closer to the surface without violating this proximity rule. However, probe-size reduction presents fabrication as well as frequency response challenges. In terms of fabrication, probe tip-surface quality is important in measurement accuracy. For two different calibration surfaces the smoother surface typically yields higher prediction accuracies. This is self-evident if one considers the fact that typical interpolation techniques use smooth continuous functions to locally model the calibration surface. The smoothness of the calibration surface depends, in turn, on the tip-surface quality. Maintaining the same relative tip-surface roughness (average tip-surface imperfection size divided by the probe diameter) becomes a fabrication challenge as the probe diameter decreases. For the present work we were able to reduce the probe diameter to as low as 0.035 in. (0.9 mm), maintaining the same high surface quality of typical 0.125-in. (3.17-mm)-diam probes. In a different challenge, as the probe diameter decreases, the tubing frequency response decreases. Because this is beyond the scope of the present work, for a treatment of this problem the reader is referred to Vijayagopal et al.[3]

Probe calibration is generally performed by placing the probe in a flowfield with known velocity magnitude and direction. The probe is pitched and yawed (or coned and rolled) through a range of angles to cover the range of possible velocity vector orientations. For each probe orientation the pressures from the five (or seven) pressure ports are recorded. This procedure is typically performed for angle increments of 2–5 deg, resulting in approximately 1000–3000 discrete calibration points, for a cone-angle range of 0–75 deg and the entire roll-angle range (0–360 deg).

After the probe has been calibrated, it can be used to measure the flow properties in an unknown flowfield. By measuring the probe port pressures at a point and comparing them to the calibration data, estimates of the flow angles and the velocity magnitude can be made. This comparison process is achieved by the calibration algorithm.

Presented as Paper 98-0204 at the AIAA 36th Aerospace Sciences Meeting, Reno, NV, Jan. 12–15, 1998; received April 8, 1998; revision received Feb. 12, 1999; accepted for publication Feb. 19, 1999.

*Assistant Professor, Department of Aerospace Engineering. Member AIAA.
†Graduate Research Assistant, Department of Aerospace Engineering.

In the present work a neural-network-based calibration algorithm was successfully developed. Before we present it, a brief overview of different types of calibration algorithms used in the past is given next.

For hemispherical probe tips one calibration method used the potential flow solution for flow over a sphere to relate flow angle and velocity to pressure differentials measured by the probe.[4] The technique was demonstrated by calibrating a hemispherical-tip five-hole probe. This method can be sensitive to construction defects of the probe tip and is generally accurate to only a few degrees at best. Interpolation techniques are widely used with multihole probe calibration data. Zilliac,[5] in his calibration of conical seven-hole probes for use in flows with large angularity, used the Akima (IMSL subroutine) interpolation procedure. For each calibration point the seven probe pressures and the total pressure are recorded along with the calculated pressure coefficients and the known roll and cone (or pitch and yaw) angles. Then, when test data are collected, the relevant coefficients are calculated and compared to the stored calibration database. By locating calibration points with pressure coefficient values similar to the measured coefficients, the approximate flow conditions are identified. The adjacent coefficient values are then interpolated to yield the precise flow properties. The technique yields good accuracy. However, the present authors' experience with the Akima interpolation procedure is that it is time consuming. This procedure is not suitable especially for applications, like air-data systems for example, where tens of readings per second are necessary.

Alternatively, empirical relationships can be derived in terms of the pressure coefficients over the different flow regions of the probe.[6] In Ref. 6 the measurement regions of a five-hole probe were divided into the low-angle regime and four high-angle regimes corresponding to the center hole and each one of the four peripheral holes, respectively. The calibration data were used to derive empirical relationships representing the pitch and yaw angles of the velocity vector in terms of the measured pressure coefficients for five-hole hemispherical probes. Using a fixed number of points, polynomial curve fits were made through the known calibration points to describe the variation of the flow variables over the measurement domain. Rediniotis et al.[7] derived bicubic polynomial fits through the calibration data for a conical seven-hole probe. Further, they increased the number of regions for which polynomials were identified. This resulted in eight low-angle regions and 32 high-angle regions, thus improving the description of the probe measurement domain. This technique guarantees agreement with the calibration points but does not necessarily ensure well-behaved calibration surfaces between calibration points.

Artificial neural networks have been effectively applied to mechanical and control systems. In aerodynamics, neural networks have proven their worthiness both as installed components in the aircraft control systems as well as research tools to investigate, model, and control fluid flows.[8–10] Neural networks were coupled with flow measurement tools such as an omnidirectional pressure probe to investigate separated and recirculating flows.[11] In the present work a novel neural-network calibration scheme has been formulated for use in the calibration of multihole pressure probes (five-hole or seven-hole). This procedure uses a large database of calibration information taken over a large range of flow cone angles (up to 75 deg). The calibration data is then used to train a multilayer neural network to predict the flow variables based on calculated pressure coefficients. During the training process, a network information file is generated that contains the necessary details of the network weights and biases. Subsequently, test data presented to the network are processed in a feedforward mode to predict the flow direction and magnitude based on the network's knowledge. This versatile technique allows for nonuniform calibration grids, dense calibration grids, and updating of the calibration data, provides high prediction accuracy, and is very fast in the feedforward mode. Also, the speed in the feedforward mode is independent of the size of the calibration file in contrast to conventional local interpolation algorithms[5,11] of similar accuracy, whose speed is highly dependent on the size of the calibration data file. Moreover, the size of the feedforward code is on the order of a hundred lines, rendering interfacing with existing user codes (such as data-acquisition and data postprocessing codes) extremely easy.

Researchers in the flight-test community have used the principles of multihole probes to develop flush air-data systems.[12–15] In these systems the nose of the aircraft is instrumented with multiple pressure ports, strategically positioned, and in essence operates as a giant multihole probe. In some efforts neural networks have been successfully used, even in real time, to extract air-data information from the pressure measurements,[16] with speeds similar to the algorithm presented here. These air-data systems have a different port arrangement than typical five- and seven-hole probes, a higher number of ports, and are not plagued by calibration issues that emerge as a result of miniaturization. Such an issue, for example, is the transportability of the calibration from one system to another. For the miniature probes discussed here, calibration transportability, without compromising measurement accuracy, is not an option, and each probe has to be calibrated individually. This is because the effect of the probe manufacturing defects on the calibration is inversely proportional to the size of the probe.

II. Miniature Pressure Probe Fabrication

In what follows the probe diameter range indicated by "miniature" is between 0.035 and 0.065 in. (0.9 and 1.65 mm). The construction of probes can be divided into the fabrication of internal and external features. The external features define the geometry exposed to the flow. The internal features define the discreet pressure channels that transmit the pressure from the probe tip to the pressure transducers.

External Features

Figure 1 illustrates the arrangement of the probe components. Probe tips are typically made of brass, with the exception of the smallest probe (0.035 in. or 0.9 mm in diameter). There are three parameters defining the tip geometry and features: 1) diameter (0.035–0.065 in. or 0.9–1.65 mm), 2) shape (conical, hemispherical, faceted), and 3) number of holes (5 or 7). The first extension (Fig. 1) precisely matches the outside diameter of the tip and is typically up to 20 diameters long. Ferrules gradually increase the outside diameter of the probe shaft, providing the strength of material necessary for a given length. If needed, a second extension can be added, creating a very long probe for special applications. Mounts are typically hexagonal to allow for probe roll referencing with the flat surfaces aligned with the hole pattern of the tip.

Internal Features

Each of the holes in the probe tip leads to a stainless-steel tube with its inside diameter matching the diameter of the hole. As the probe shaft diameter increases, each tube is telescoped into a larger tube, which finally protrudes from the back of the mount. Each connection is soldered and tested for strength and leakage. The final assembly is also tested for pressure cross-talk, i.e., pneumatic communication between two or more probe holes and their associated tubing. Pictures of the miniature probes fabricated at the Aerospace Engineering Department of Texas A&M University are shown in Figs. 2a–2g. Figure 2a shows a probe with conical tip, 0.035 in. (0.9 mm) in diameter, whereas Fig. 2b shows a faceted tip, 0.065 in. (1.65 mm) in diameter (in all pictures, the coin is a dime). Figure 2c is an assortment of probes with conical and hemispherical tips, 0.035, 0.065, and 0.125 in. (or 0.9, 1.65, and 3.17 mm) in diameter. Figures 2d–2f show different zoomed-in views of a probe with a conical tip, 0.04 in. (1 mm) in diameter. Figure 2g shows the end view of a hemispherical five-hole probe with tip diameter 0.065 in. (1.65 mm).

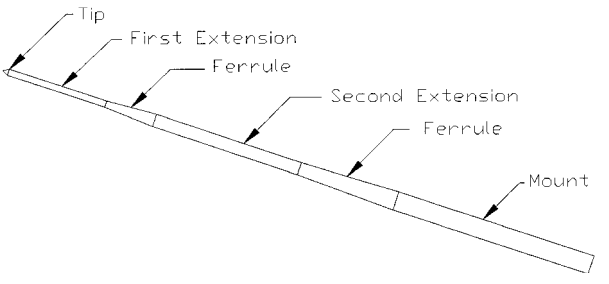

Fig. 1 Schematic of miniature probe assembly.

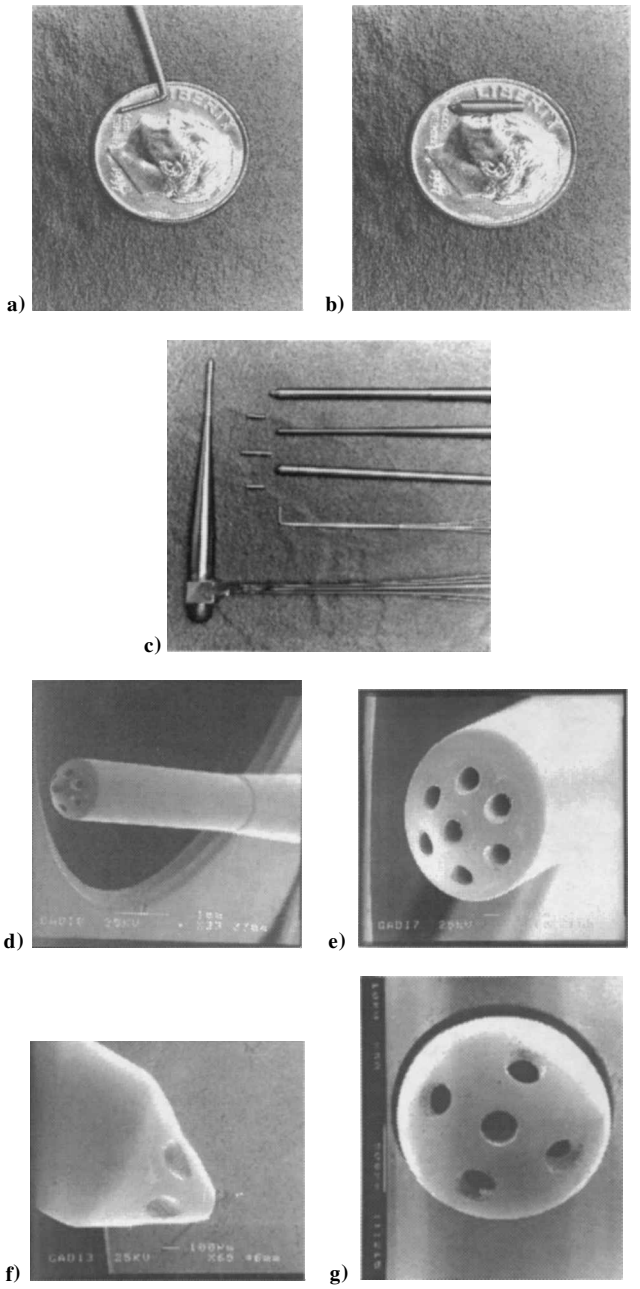

Fig. 2 Miniature probe pictures: a) probe with conical tip, 0.035 in. (0.9 mm) in diameter; b) faceted probe tip, 0.065 in. (1.65 mm) in diameter; c) assortment of probes with various tip geometries; d) electron microscope picture of probe with conical tip, 0.04 in. (1 mm) in diameter; e) and f) closer tip views for the probe of Fig. 2d; and g) electron microscope picture of hemispherical tip, 0.065 in. (1.65 mm) in diameter.

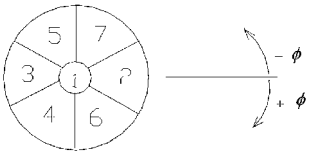

Fig. 3 Seven-hole measurement domain divided into seven sectors, each centered on an individual pressure port numbered 1–7.

III. Probe Calibration Background

A brief overview of the probe calibration theory is given next for the case of the seven-hole probe. The flow over a seven-hole probe can be typically divided into two regimes: low-angle and high-angle flow. The low-angle flow regime is defined as the velocity inclination range for which the pressure registered by hole #1 (Fig. 3) is the highest among the seven measured pressures. The flow remains attached over the entire probe; therefore, a unique set of seven pressures exists at every probe orientation with respect to the flow. The

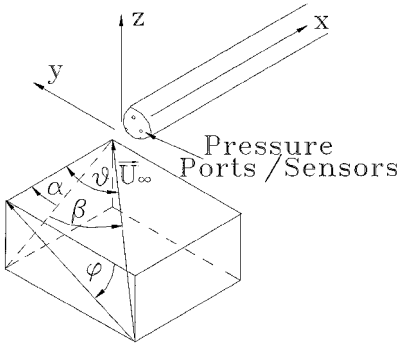

Fig. 4 Flow angle and probe coordinate system definition.

orientation of the probe with respect to the flow is defined by two angles: the pitch-angle α and the yaw-angle β (Fig. 4). For high-angle flows the ith hole registers the maximum pressure p_i, where i takes a value from 2 through 7. The flow may not be attached over the entire probe. For high-angle flows the position of the probe with respect to the flow is more conveniently defined in spherical coordinates. The two orientation angles are the cone-angle θ and the roll- angle ϕ (Fig. 4).

At every measurement location in a flow-mapping experiment, the local velocity vector can be fully characterized by four variables. In the low-angle regime the variables are pitch-angle α, yaw-angle β, total pressure coefficient A_t, and the static pressure coefficient A_s. In the high-angle regime the four variables are cone-angle θ, roll-angle ϕ, and the pressure coefficients A_t and A_s. Knowledge of the local temperature is also required; however, for the flows of interest here the temperature is constant and equal to the freestream temperature, which is measured and known. The four variables need to be determined as functions of the measured pressures or the two nondimensional pressure coefficients formed from these pressures: B_p, B_y for low-angle flow and B_c, B_r for high-angle flow. The definitions are as given next.

Low-Angle Regime (Sector 1)
Independent (Input) Variables:

$$B_p = \frac{1}{\sqrt{3}} \cdot \frac{(p_7 + p_5 - p_4 - p_6)}{q}$$
$$B_y = \frac{(p_2 - p_3)}{q} + \frac{(p_6 - p_5 + p_7 - p_4)}{2 \cdot q} \tag{1}$$

Dependent (Output) Variables:

$$A_t = \frac{(p_1 - p_t)}{q}, \qquad A_s = \frac{(p_1 - p_s)}{q}$$
$$\text{Pitch-angle, } \alpha \qquad \text{Yaw-angle, } \beta \tag{2}$$

where $q = p_1 - [(p_2 + p_3 + p_4 + p_5 + p_6 + p_7)/6]$, p_t is the local total pressure, and p_s is the local static pressure.

High-Angle Regimes (Sectors 2–7)
Independent (Input) Variables:

$$B_c = \frac{(p_i - p_1)}{q}, \qquad B_r = \frac{(p^+ - p^-)}{q} \tag{3}$$

Dependent (Output) Variables:

$$A_t = \frac{(p_i - p_t)}{q}, \qquad A_s = \frac{(p_i - p_s)}{q}$$
$$\text{cone-angle, } \theta \qquad \text{roll-angle, } \phi \tag{4}$$

where $q = p_i - [(p^+ + p^-)/2]$ and p_i is the highest measured pressure (at the ith port). Looking into the probe tip, p^+ and p^- are the

pressures measured by the peripheral holes adjacent to port i in the clockwise and counterclockwise direction, respectively.

IV. Artificial Neural-Network Architecture, Training, and Optimization

Network Architecture

An artificial neural network is composed of processing elements called nodes, with each node having several input branches but only one output branch. Each input connection to a node has a weight associated with it. The input values are multiplied by the associated weights and summed together with a node bias value. An activation function then acts on the summed value producing the output value for the node. An artificial neural network is built of several layers of nodes with the first layer typically having as many nodes as there are input variables. The number of middle or hidden layers is application dependent. Figure 5 shows a typical network structure, which could be used to train and predict the pitch-angle. All of the node interconnections are shown. The input layer accepts two input elements. There are two hidden layers and one output layer. The output of each node in a layer serves as input to the nodes of the next layer. In Fig. 5, $f1$–$f9$ are the activation functions applied at each node.

A node's output o_i^h is given by

$$x_i^h = \sum_j w_{ij}^h o_j^{h-1}, \qquad o_i^h = f_i^h\left(x_i^h\right) \tag{5}$$

where superscript h denotes the layer number, subscript i denotes the node in question, and subscript j denotes the node in the previous $(h-1)$ layer.

The artificial neural-network algorithm that has been developed uses coefficients calculated from probe calibration pressure data for the training of a set of neural networks. For the seven-hole probe each network uses two system inputs, the two pressure coefficients B_p (or B_c), B_y (or B_r), and four system outputs, A_t, A_s, pitch α (or cone θ), and yaw β (or roll ϕ) angles. A large training set of data containing cone and roll angles and the pressure information is taken using a calibration apparatus.[11] The pressures are reduced to the relevant pressure coefficients. The network uses this information as its training data and, through a training algorithm, adjusts its weights to minimize the resultant error between the predicted and the exact values of the outputs. Once the network is trained, measured pressure data that may or may not coincide with the training data can be input to the network, which then predicts the flow variables (velocity and angles) corresponding to the measured pressures.

If the high-angle sectors were further split up to improve the description of the measurement domain as shown in Fig. 6, higher prediction accuracy could be achieved. This was expected from our previous neural-network experience in which it became repeatedly obvious that, the more complicated the function to be represented and the bigger its definition domain, the harder the task of finding a neural network with high modeling accuracy. So the high-angle

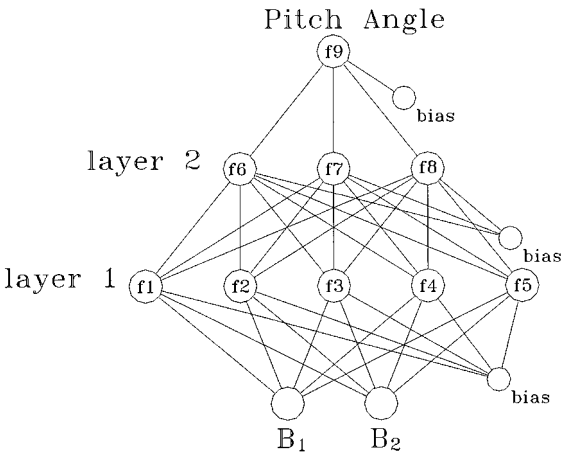

Fig. 5 Typical network structure that takes a two-element input to train for and predict the pitch-angle.

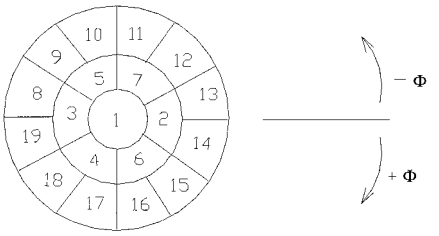

Fig. 6 Seven-hole domain split up to enhance neural-network performance.

sectors were first split into low–high and high–high regimes. The high–high regimes were further split laterally (in roll). For example, sector 2 of Fig. 3 was replaced by three such subsectors in Fig. 6: 2 (low–high), and 13, 14 (high–high). In this way a seven-hole probe was split up to have as many as 19 sectors. Care was taken to ensure that there was at least a 5-deg overlap (in cone and roll) between adjacent sectors. This is done to deal with calibration and test points that lie near the borders of adjacent sectors.

Artificial Learning

An artificial neural network learns by adjusting the values of its weights through a training process. The training process consists of giving the neural-network sample input-output data pairs and letting the neural-network algorithm adjust the weights until it can produce the correct output for each input. This procedure is called *supervised learning*. Backpropagation is one method of self-correction. During this process, input is applied to the first layer of a neural network and propagated through until an output is generated at the last layer of the neural network. The output obtained through forward propagation is then compared with the desired output to generate an error signal. The error is then distributed back to the nodes of the previous layer according to their contribution to the error. This process is repeated for all layers, updating the weights. The neural network is iteratively trained with several input-output vector sets until it has all of the training data encoded into it. Once the network has correctly encoded the training data, it can process input data according to the parameters set forth by the training process. It is important to note that the trained neural network will perform only as well as the training data allows. For this reason, care should be taken in selecting the set of training vectors.

Typically, the question of error convergence to a local or global minimum arises. If the backpropagation algorithm converges to a local minimum, learning will then cease, and the error of the network output may be unacceptably high. Two simple methods of dealing with this circumstance are to increase the number of hidden layers or to start over the training process with a different set of initial weights. When the backpropagation algorithm does reach an acceptable solution, there is no guarantee that it has reached the global minimum. But as long as the solution is acceptable from an error standpoint, convergence to a local minimum is irrelevant. To avoid the situation of the algorithm converging to a local minimum without reaching a desired minimum error, momentum learning was implemented in the code. Momentum learning allows the network to respond, not only to the local gradient of the error surface, but also to recent trends in the error surface. The algorithm is thus less likely to get trapped in local minima. To speed up convergence, adaptive learning was also implemented. Adaptive learning allows the learning rate to vary depending on the output error. This allows the network to adapt the learning rate to the local terrain of the error surface. When a larger rate is possible for stable learning, the rate is increased. When smaller learning rate is required, the rate is automatically decreased.

The training algorithm accepts as its input a raw pressure data file containing the calibration data for the probe. This data file is then converted to training vector files for every sector of the probe. The training vector files are used to train the neural networks by backpropagation. Weight initialization is performed either by generating random weights or by using existing weights files from previously trained similar networks. During training, the weight matrices are updated using a steepest descent technique to progress toward the

minimum error. The error is calculated at each node on the output layer as the difference in the predicted and known outputs:

$$\delta_k^H = \frac{\mathrm{d}f_k^H\left(x_k^H\right)}{\mathrm{d}x_k^H}\left(o_k^H - \text{known}\right) \tag{6}$$

where δ_k^H is the error sensitivity for node k on the output layer H. The error is backpropagated through the network by the following recurrence relation[17–20]:

$$\delta_i^{h-1} = \frac{\mathrm{d}f_i^{h-1}\left(x_i^{h-1}\right)}{\mathrm{d}x_i^{h-1}} \sum_k w_{ki}^h \delta_k^h, \qquad h = 2 \ldots H \tag{7}$$

For each of the nodes in the hidden layers, δ_i^h represents the contribution of error to the network output. The weight changes at each node are then calculated by the following learning rule[18]:

$$\Delta w_{ij}^h(t+1) = \alpha \Delta w_{ij}^h(t) + (1-\alpha)\eta \delta_i^h o_j^{h-1} \tag{8}$$

where $\Delta w_{ij}^h(t)$ is the change in weights for layer h at iteration t, o_j^{h-1} is the output of node j on layer $h-1$, and $\delta_i^h o_j^{h-1}$ is the estimated error gradient calculated for each weight, which can be expressed as

$$\frac{\partial \hat{e}}{\partial w_{ij}^h} = \delta_i^h o_j^{h-1} \tag{9}$$

As already mentioned, to aid in convergence a momentum term α is used to dampen the oscillations in the convergence and the adaptive learning rate term, η is used as a type of dynamic over- and under-relaxation for updating the weight matrices. The learning rate is increased, and the weights are updated after each iteration that reduces the sum-squared error $\hat{e}$ of the network. After each unsuccessful iteration the learning rate is decreased, and the weight changes are discarded.

To further improve the convergence rate, the Levenberg–Marquardt optimization method was implemented[21]:

$$\Delta \boldsymbol{W} = (\boldsymbol{J}^T \boldsymbol{J} + k\boldsymbol{I})^{-1} \boldsymbol{J}^T \boldsymbol{E} \tag{10}$$

Here $\boldsymbol{J}$ is the error Jacobian matrix consisting of the partial derivatives of the error terms with respect to the node weights, k is a scalar, and $\boldsymbol{E}$ is the error vector determined from the known vector output and the network calculated values. When k is large, the expression is approximately the gradient descent method. When k is small, the expression approximates the Newton method.[20] Because the second method is faster but tends to be less accurate when near an error minimum, the scalar k is adjusted like the adaptive learning rate. As long as the error decreases, k is made larger. If the error increases, k is made smaller. Further, residual monitoring and active perturbation of the weight matrices are additional methods used by the algorithm to ensure satisfactory convergence and to stimulate learning.

Network Optimization

Different network architectures will obviously produce different levels of prediction accuracy. Procedures to find the optimum network structure for specific problems have so far been primarily based on trial and error. Ideally, the neural-network code should develop its own intelligence and experience in deciding on the optimum architecture rather than the user being tied to hours of tedious, manual interrogation. In the present code, although the user can at any time override the code's decisions, an expandable heuristic rule base is incorporated that guides the algorithm in the optimal network selection. The main function of these rules is to associate a certain problem or a certain class of problems to certain optimal network architecture or a range of optimal architectures. The main function of the code's optimizer is to generate and train different network architectures and, by comparing their relative performance for a specific problem, conclude on a set of optimal architectures. It can generate optimal network architectures for five-hole probes, seven-hole probes, conical, hemispherical, and faceted tip geometries and spherical omniprobes. For the probes calibrated here the typical optimal architecture consisted of one input layer, two hidden layers, and one output layer; and the number of nodes per hidden layer were typically eight and four for the first and second hidden layer, respectively. The activation functions that worked the best were linear, sine, cosine, hyperbolic tangent, and sigmoid.

V. Calibration Hardware and Setup

Pressure data acquisition during probe calibration and use was performed with a 32-transducer electronic pressure scanner (ESP) from PSI, Inc., with a pressure range of ±10 in H_2O. The ESP was interfaced to a laboratory computer and was calibrated on-line. The calibration was performed using the apparatus described in Kinser and Rediniotis.[11] A 16-bit A/D board from ComputerBoards was used to perform data acquisition. A dual-axis stepper-motor assembly, which is computer controlled, can vary the cone and roll angles (θ, ϕ) in the ranges (0, 180 deg) and (−180, 180 deg), respectively. The positioning resolution for the calibration assembly is 0.32 deg in cone and 0.9 deg in roll. To be able to assess the accuracy of the calibration technique, test data were also collected, which involved positioning of the probe at several known orientations, $(\alpha_{\text{test}}, \beta_{\text{test}})$ or $(\theta_{\text{test}}, \phi_{\text{test}})$, none of them coincident with any of the orientations used for calibration, $(\alpha_{\text{cal}}, \beta_{\text{cal}})$ or $(\theta_{\text{cal}}, \phi_{\text{cal}})$, and collection of the pressures. These pressures were fed into the calibration routines, and a predicted pair $(\alpha_{\text{pred}}, \beta_{\text{pred}})$ or $(\theta_{\text{pred}}, \phi_{\text{pred}})$ was calculated. The difference between the two pairs $(\alpha_{\text{test}}, \beta_{\text{test}})$ and $(\alpha_{\text{pred}}, \beta_{\text{pred}})$ or $(\theta_{\text{test}}, \phi_{\text{test}})$ and $(\theta_{\text{pred}}, \phi_{\text{pred}})$ is a measure of the calibration accuracy, although some bias errors are not included (for example, because of tunnel flow angularity, as seen later in Sec. VI).

Calibration and data acquisition were performed in the Texas A&M 3 × 4 ft Aerospace Engineering Wind Tunnel. This is a closed circuit tunnel with a test section equipped with a breather so that the static freestream pressure is equal to the control room pressure. The clear Plexiglas® test section is 4 ft (1.22 m) wide, 3 ft (0.91 m) tall, and 6 ft (1.83 m) long. The contraction ratio is 9:1. The maximum speed achieved in the tunnel is about 150 ft/s (45.7 m/s) with freestream turbulence less than 0.16%. To avoid temperature fluctuations over time, there is an active cooling system to keep the freestream temperature at 60°F (15.6°C) during testing.

VI. Discussion of Results and Error Analysis

One of the salient features of the calibration algorithm developed is the range of available control over the network architecture. Typical commercial codes allow for an input layer; a few hidden layers (limited number), each one with a specific activation function for the entire layer; and an output layer with its activation function. The code developed here allows the user to specify different activation functions at each node. The activation functions $f1$–$f9$ in Fig. 5 can be selected from a database of functions or can be user-defined. These functions include constant, linear, quadratic, cubic, logsig, tansig,[17] cosine, sine, and exponential functions. These functions can be customized and the user can define new activation functions.

To assess the effect of using multiple activation function within a layer, two types of network architectures were trained on data from analytical polynomials and actual probe calibration data. The first architecture had one type of activation function per layer, whereas the second employed multiple functions within a layer. Both network architectures were optimized through the algorithm's optimizer. In the first network architecture the network with the best performance was found to have the following structure: four layers, three of which are hidden, each with a single activation function, linear, quadratic, and cubic, respectively. The optimal network of the second type was a simpler two-layer network. Its single hidden layer used three different node types: linear, quadratic, and cubic. Both architectures have the ability to model a cubic polynomial selected for this test. However, the multifunction network requires only 2 layers, 4 nodes, and 10 weights to achieve better results than the 4-layer, 10-node, 34-weight single-function layer network. The convergence rate for the multifunction network is markedly better as Fig. 7 illustrates. Of the two architectures, multifunction layer networks have been consistently found to have higher convergence rates and converge to lower error levels.

Once the network has been trained to a satisfactory level of convergence, an output binary file is then created, which contains all of the trained network information. This binary file is used by the feed-forward procedure for reducing any new pressure data acquired with the calibrated probe to the velocity components and the orientation

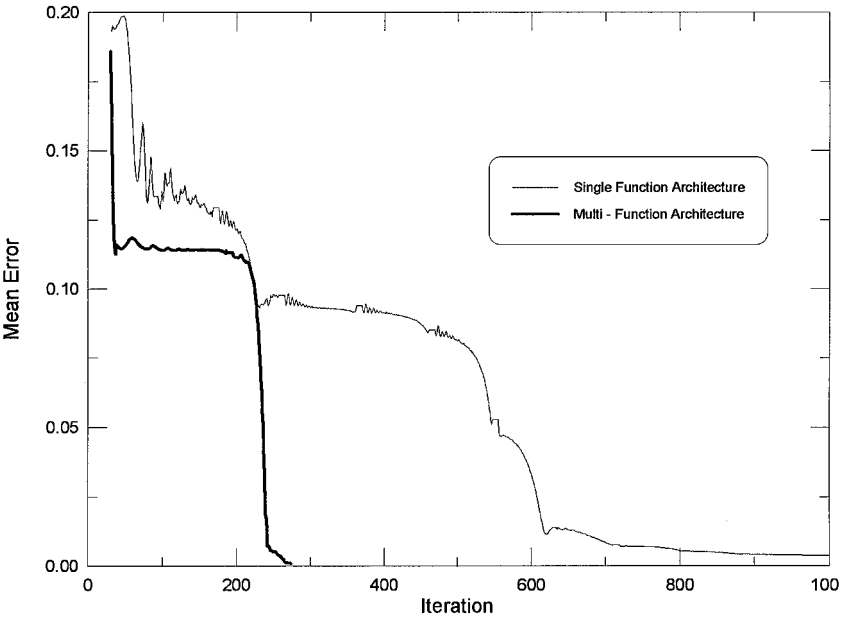

Fig. 7 Convergence history for single and multiple activation function architectures.

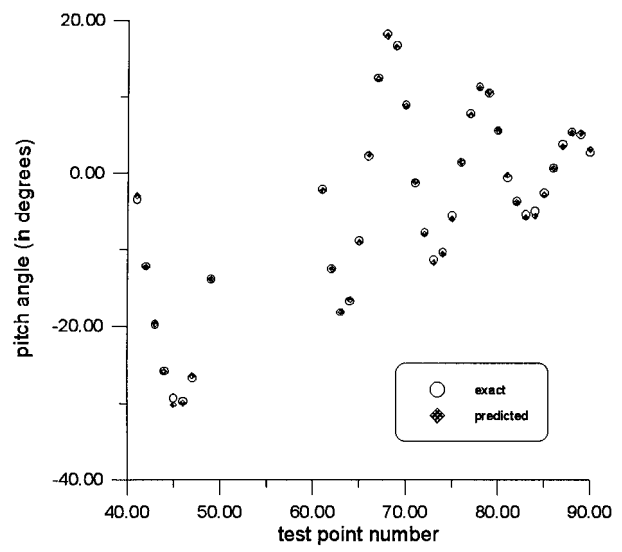

a) Pitch-angle

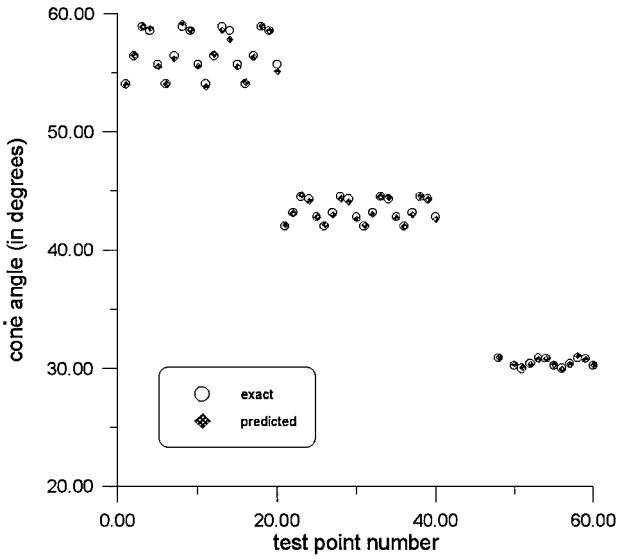

c) Cone-angle

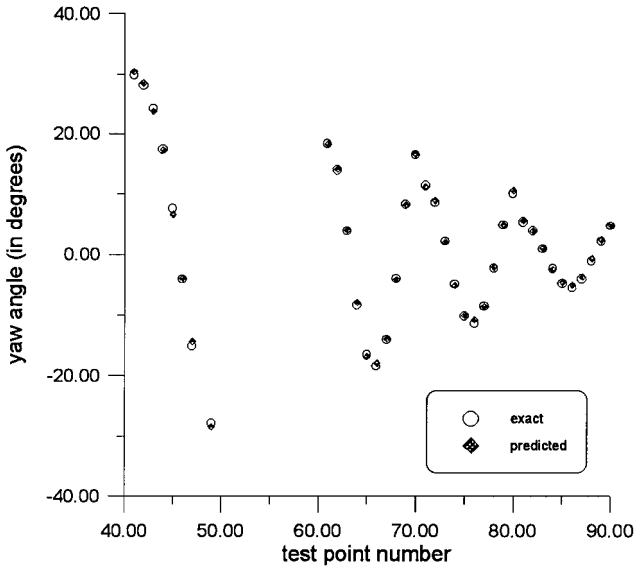

b) Yaw-angle

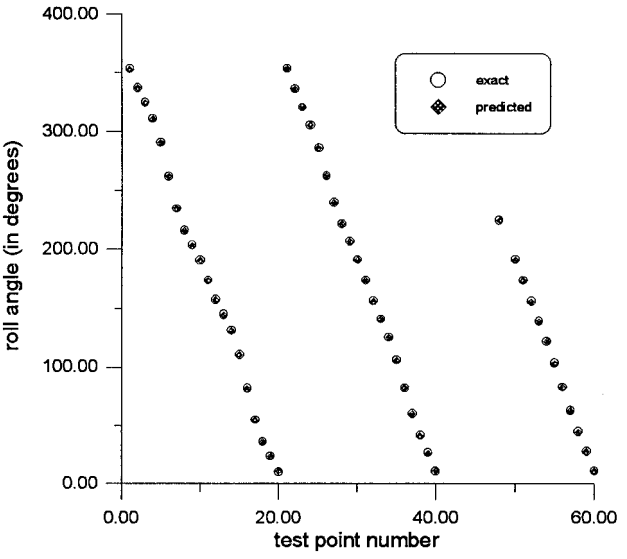

d) Roll-angle

Fig. 8 Neural-network prediction results.

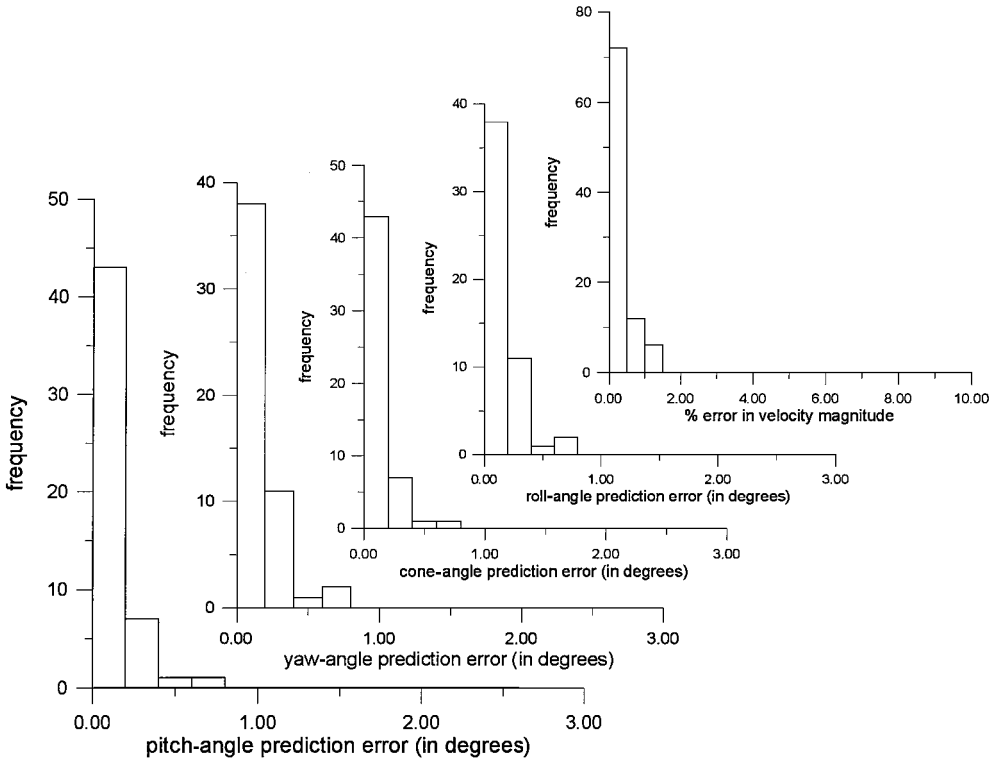

Fig. 9 Prediction error histograms for pitch, yaw, cone, and roll-angle and velocity magnitude.

angles. This feedforward mode is exceptionally fast as compared to similar accuracy local least-squares interpolation techniques[11] and is not dependent on the size of the calibration data file. Typically, the neural-network code can reduce a test data file that contains 100 test points in just about 5 s, whereas the same test file may take about a minute to be processed by the local least-squares interpolation technique. As mentioned in the Introduction, this increased data reduction rate of the neural-network algorithm makes it suitable for applications like air-data systems, where several readings per second are required.

A miniature conical seven-hole probe, 0.063 in. (1.6 mm) in diameter was calibrated at a freesteam velocity of 70 ft/s (21.3 m/s). The high-angle sectors were split up as already described to enhance the performance of the networks. Figures 8a–8d show the predictions for the flow angles both in low-angle and high-angle sectors. Typical calibration performance results are shown in Fig. 9 in the form of error histograms. The error is represented along the horizontal axis, while the vertical axis (labeled *frequency*) represents the number of points in a specific error bin. The error band of a specific bin is indicated by the width of the corresponding vertical bar. From these histograms the following error statistics can be calculated: pitch-angle—average absolute error = 0.22 deg, standard deviation of error = 0.26 deg; yaw-angle—average absolute error = 0.28 deg, standard deviation of error = 0.34 deg; cone-angle—average absolute error = 0.15 deg, standard deviation of error = 0.18 deg; roll-angle—average absolute error = 0.17 deg, standard deviation of error = 0.21 deg; and velocity magnitude—average absolute error = 0.35%, standard deviation of error = 0.52%. The higher error levels in the pitch- and yaw-angle prediction (low-angle sector), as compared to the error levels in the cone- and roll-angle prediction (high-angle sectors), are due to the fact that each of the high-angle sectors was further split up to several subsectors, and each subsector was calibrated individually, while no such subdivision was applied to the low-angle sector.

The uncertainty analysis presented next is based on the techniques discussed in Ref. 22, and the application of the techniques to the multihole probe problem follows the procedures discussed in Ref. 23. First, the uncertainty of the pressure measurement hardware is estimated. The pressure scanner used was calibrated during calibration of the probe, on-line, every hour. A 5-point calibration was performed, which accounted for transducer nonlinearities. The reference manometer used for calibration had an uncertainty of 0.005 torr for the range of pressures used here (±6 torr). The preceding combination, along with a one-count A/D conversion uncertainty of the 16-bit A/D board, yielded a pressure measurement worst-case error of 0.015 torr or 0.009 in H_2O. Errors in angular positioning were negligible. The resolution of the cone- and roll-positioning stepper motors (0.32 and 0.9 deg) should not be confused with their positioning precision, which is on the order of arc seconds. Slipping of the stepper motors could of course compromise the accuracy, especially because no angular positioning encoders were employed. However, strong evidence (although not absolute proof) that no slipping occurred was the fact that at the end of a calibration session the stepper motors returned the probe, as instructed, to the exact orientation that it started from at the beginning of the session. If any slipping had occurred, it should have happened in a fashion such that all slipping occurrences canceled themselves out, which is a very unlikely event. Bias errors because of probe sting deflection were also negligible at the speeds of calibration and for the specific structural design of the sting. Uncertainty in the tunnel flow angularity will cause a bias error if the probe is tested or used in a different facility. However, for the calibration test processes followed in this work, as described in Sec. V, flow angularity does not have an effect for the following reason. Both calibration and test data were taken in the same facility and freestream velocity, and the calibration apparatus was designed such that it maintained the probe tip always at the same location, regardless of probe orientation.

The uncertainty in the evaluation of the pressure coefficients B_p, B_y, B_c, B_r, A_t, A_s was calculated using their definition formulas (1)–(4) and constant-odds combination[22] given by

$$\delta C_p = \sqrt{\sum_i \left(\frac{\partial C_p}{\partial p_i} \delta p_i \right)^2} \tag{11}$$

where C_p is any of the pressure coefficients and δp_i is the uncertainty in the measurement of pressure p_i. Subsequently, and to see how the uncertainty in the calculation of the pressure coefficients propagates through the neural-network technique, a jitter approach[22] was followed. The estimates of the δp_i were obtained from a Gaussian

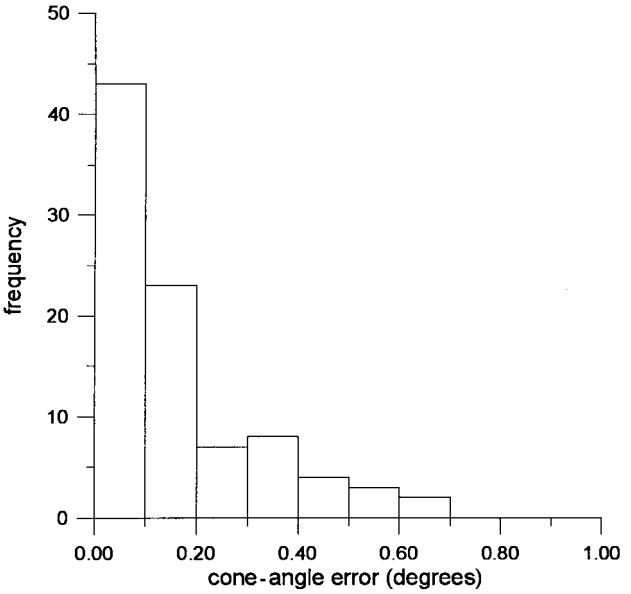

a) Cone-angle error

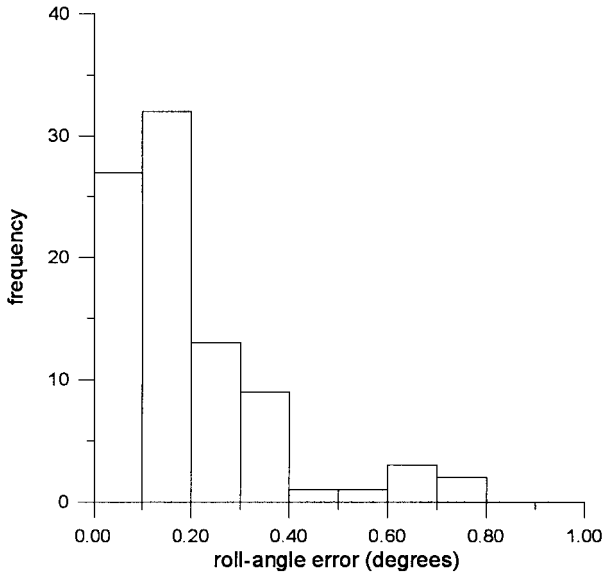

b) Roll-angle error

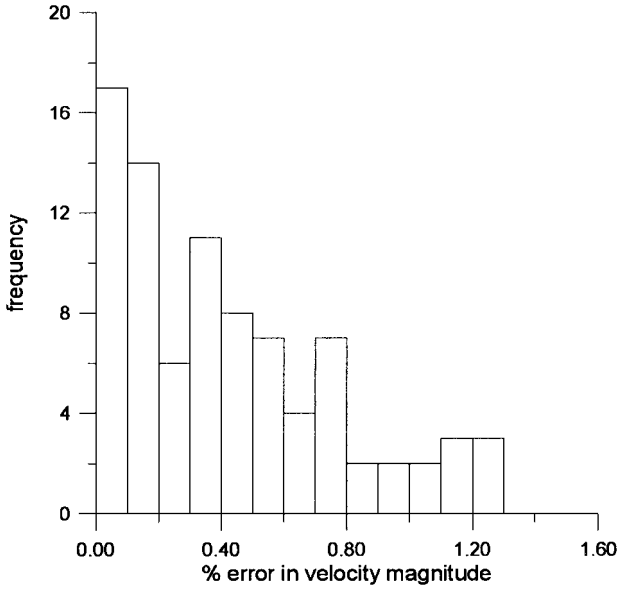

c) Velocity-magnitude error

Fig. 10 Error histograms derived from uncertainty analysis.

distribution with zero mean and a standard deviation of 0.005 torr. This was chosen so that the worst-case error in pressure measurement, i.e., 0.015 torr, corresponds to three standard deviations from the mean, which in turn corresponds to a 99.5% probability that the pressure measurement error is smaller or equal to 0.015 torr. The preceding allowed the estimation of uncertainty in B_p (or B_c), B_y (or B_r), A_t, and A_s for every calibration and test point through Eq. (11). The obtained δB_p (or δB_c), δB_y (or δB_r), δA_t, and δA_s were used to perturb the original values of these coefficients for the calibration points, and the perturbed values were subsequently used as the inputs to train the neural networks. Once the networks were trained, they were used to reduce the test data that were also perturbed in the manner just explained. The predictions obtained in this process were compared to those obtained from the unperturbed networks and test points, and the standard deviation of the differences between these two yielded estimates for the overall uncertainty. The results are listed here: standard deviation in cone-angle errors, 0.24 deg; standard deviation in roll-angle errors, 0.37 deg; and standard deviation in velocity magnitude error, 0.72%.

Figure 10 shows the histograms of these errors. The statistical properties of these histograms are very similar to the ones obtained from the actual calibration tests (Fig. 9). As already seen, the error levels obtained from the actual test are within those predicted from the uncertainty analysis. The uncertainty analysis presented here applies strictly to steady-state flows. The issues of probe calibration and measurement accuracy in unsteady flow environments are addressed elsewhere.[3,24]

VII. Conclusion

Miniature multihole probes were successfully designed and fabricated with high tip-surface quality. Five- and seven-hole miniature probes were fabricated with hemispherical, conical, and faceted tip geometries and tip diameters as low as 0.035 in. A neural-network-based probe calibration algorithm was developed. The algorithm's features include flexibility in network architecture design and network self-optimization capabilities. The introduction of multiple activation function architectures had a significantly positive impact on the network training convergence rates and levels. In the feedforward mode the algorithm yields computational speeds an order of magnitude higher than those typically achieved by similar accuracy interpolation algorithms. Moreover, the small size of the feedforward code facilitates its formulation into a subroutine and enhances its ease of interfacing with other software. A miniature seven-hole probe was calibrated and tested in the wind tunnel. The new algorithm combined with precision probe calibration hardware and procedures yielded prediction accuracies of 0.28 deg in the angle prediction and 0.35% in the velocity magnitude prediction. Finally, an error analysis was performed on the calibration procedures and algorithm and yielded uncertainty levels compatible with those produced by the actual probe test.

Acknowledgments

This work was supported by NASA Langley Research Center, Flow Modeling and Control Branch, with William Sellers as Monitor, under Grant NAG-1-1753, and by Aeroprobe Corporation under Project 32525-52050. The authors would like to gratefully acknowledge the contribution of Richard Allen, whose machining dexterity made the fabrication of the miniature probes possible.

References

[1]Rediniotis, O. K., "The Transient Development of Vortices over a Delta Wing," Ph.D. Dissertation, Dept. of Engineering Science and Mechanics, Virginia Polytechnic Inst. and State Univ., Blacksburg, VA, Oct. 1992.

[2]Hoang, N. T., "The Hemisphere-Cylinder at an Angle of Attack," Ph.D. Dissertation, Dept. of Engineering Science and Mechanics, Virginia Polytechnic Inst. and State Univ., Blacksburg, VA, Dec. 1991.

[3]Vijayagopal, R., Pathak, M. M., and Rediniotis, O. K., "Miniature Multi-Hole Pressure Probes—Their Neural Network Calibration and Frequency Response Enhancement," AIAA Paper 98-0204, Jan. 1998.

[4]Kjelgaard, S. O., "Theoretical Derivation and Calibration Technique of a Hemispherical-Tipped, Five-Hole Probe," NASA TM-4047, Sept. 1988.

[5]Zilliac, G. G., "Calibration of Seven-Hole Probes for Use in Fluid Flows with Large Angularity," NASA TM-102200, Dec. 1989.

[6]Bryer, D. W., and Pankhurst, R. C., "Pressure-Probe Methods for Determining Wind Speed and Flow Direction," Her Majesty's Stationery Office, London, 1971.

[7]Rediniotis, O. K., Hoang, N. T., and Telionis, D. P., "The Seven-Hole Probe: Its Calibration and Use," *Forum on Instructional Fluid Dynamics Experiments*, edited by C. Dutton, Vol. 152, American Society of Mechanical Engineers, Washington, DC, 1993, pp. 21–26.

[8]Schreck, S. J., Faller, W. E., and Luttges, M. W., "Neural Network Prediction of Three-Dimensional Unsteady Separated Flow Fields," AIAA Paper 93-3426, Aug. 1993.

[9]Schreck, S. J., and Faller, W. E., "Encoding of Three-Dimensional Unsteady Separated Flow Field Dynamics in Neural Network Architectures," AIAA Paper 95-0103, Jan. 1995.

[10]Fan, X., Herbert, T., and Haritonidis, J. H., "Transition Control with Neural Networks," AIAA Paper 95-0674, Jan. 1995.

[11]Kinser, R. E., and Rediniotis, O. K., "Development of a Nearly-Omni-Directional, Three Component Velocity Measurement Pressure Probe," AIAA Paper 96-0037, Jan. 1996.

[12]Larson, T. J., Whitmore, S. A., Ehernberger, L. J., Johnson, J. B., and Siemers, P. M., "Qualitative Evaluation of a Flush Aft Data System at Transonic Speeds and High Angles of Attack," NASA TP-2716, June 1987.

[13]Larson, T. J., Moes, T. R., and Siemers, P. M., "Wind Tunnel Investigation of a Flush Airdata System at Mach Numbers From 0.7 to 1.4," NASA TM-101697, Sept. 1990.

[14]Whitmore, S. A., Davis, R. J., and Fife, J. M., "In-Flight Demonstration of a Real-Time Flush Airdata Sensing System," *Journal of Aircraft*, Vol. 33, No. 5, 1996, pp. 970–977.

[15]Whitmore, S. A., Cobleigh, B. R., and Haering, E. A., "Design and Calibration of the X-33 Flush Airdata Sensing System," NASA TM-1998-206540, Jan. 1998.

[16]Rohloff, T. J., "Development and Evaluation of Neural Network Flush Airdata Sensing Systems," Ph.D. Dissertation, Dept. of Mechanical Engineering, Univ. of California, Los Angeles, CA, May 1998.

[17]Freeman, J. A., and Skapura, D. M., *Neural Networks Algorithms, Applications and Programming Techniques*, Addison–Wesley, Reading, MA, 1992.

[18]Fausett, L., "Fundamentals of Neural Networks Architectures, Algorithms, and Applications," Prentice–Hall, Englewood Cliffs, NJ, 1994.

[19]Hagan, M., Demuth, H., and Beale, M., *Neural Network Design*, PWS Publishing, Boston, MA, 1996.

[20]Hassoun, M. H., *Fundamentals of Artificial Neural Networks*, MIT Press, Cambridge, MA, 1995.

[21]Demuth, H., and Beale, M., "MATLAB Neural Network Toolbox," The Mathworks, Inc., Natick, MA, 1997.

[22]Moffat, R. J., "Contributions to the Theory of Single-Sample Uncertainty Analysis," *Transactions of the ASME*, Vol. 104, June 1982, pp. 250–258.

[23]Zilliac, G. G., "Modeling, Calibration, and Error Analysis of Seven-Hole Pressure Probes," *Experiments in Fluids*, Vol. 14, No. 1/2, 1993, pp. 104–120.

[24]Rediniotis, O. K., Johansen, E., Tsao, T., Seifert, A., and Pack, L., "MEMS-Based Probes for Velocity and Pressure Measurements in Unsteady and Turbulent Flowfields," AIAA Paper 99-521, Jan. 1999.

J. Seitzman
Associate Editor